

NUMERICAL SIMULATION OF 3D PRINTED ULTRA HIGH-PERFORMANCE CONCRETE USING THE LATTICE DISCRETE PARTICLE MODEL

BAHAR AYHAN*, ELMER M. IRIZARRY*, EROL LALE*, KE YU*, MATTHEW TROEMNER[†] AND GIANLUCA CUSATIS*

* Northwestern University, Department of Civil and Environmental Engineering, Evanston, IL 60208, USA
e-mail: bahar.ayhan@northwestern.edu

[†]North Fracture Group, Houghton, MI 49931, USA

Key words: 3D Printing, concrete construction, material parameters, structural performance, LDPM

Abstract. The Lattice Discrete Particle Model (LDPM) is highly effective in capturing the fracture behavior of concrete, especially at the scale where significant material heterogeneities, such as coarse aggregates, dominate. This model constructs a meso-structure of concrete using a stochastic approach to generate spherical particles. This process is guided by several key parameters, including cement content, water-to-cement ratio, and the size range of aggregates, from the largest to the smallest. Delaunay tetrahedralization is employed to establish the lattice framework, targeting the centers of aggregates, which results in formation of polyhedral cells surrounding each aggregate particle through a 3D domain tessellation. LDPM is integrated into Project Chrono, an open-source multi-physics simulation engine and implemented as a user element code in Abaqus. In this study, mechanical characterization of the 3D printed concrete samples will be investigated. A 3D scanner is utilized to ensure accurate geometric representation of the printed sample geometries, which are then imported into the FreeCAD preprocessor for meso-structure generation. The simulations of various mechanical tests are conducted, such as unconfined compression and three-point bending tests, with the ability to apply loads at different orientations relative to the printing direction. The model's accuracy is validated by comparing the simulation results with experimental data, ensuring that it can accurately capture the behavior of 3D printed ultra-high-performance concrete under different loading conditions.

1 INTRODUCTION

3D concrete printing has experienced rapid growth in recent years, increasing the need for advancements in design, construction, and quality assurance technologies. However, the hardened behavior of printed concrete exhibits anisotropy, complicating comparisons with standardized tests, as cast samples fail to replicate the behavior of printed specimens. Despite progress in experimental characterization, the concrete 3D printing industry will not

achieve its full potential without robust numerical models to guide decisions regarding design. The printing process involves numerous variables affecting mechanical performance, and current numerical models fall into three main categories: continuum-based, interface-based, and discrete methods [1].

Continuum-based models overlook printed layers, using simplified techniques to model anisotropy, and struggle to represent interface zones and complex effects [2]. Interface-based

models account for anisotropy through adhesive properties of the interface but rely on simplified damage laws, limiting their applicability [3]. Discrete models, which can account for discontinuous and heterogeneous effects of concrete and other quasi-brittle materials, have been implemented in 3D printed concrete applications in the form of discrete element method (DEM) [4], and lattice models [5]. One of the powerful discrete model, Lattice Discrete Particle Model (LDPM), which has been successfully used in modeling concrete in a wide array of loading configurations [6–10]. It provides detailed insights into modeling heterogeneous material behavior, offering higher accuracy with a reasonable computational cost [6, 7].

The motivation for this research study is to provide steps which help bridge the gap between large scale structural testing and small scale mechanical characterization of 3D printed concrete. We introduce a methodology to evaluate strength of printed concrete samples while preserving surface geometry, crucial for capturing crack initiation and propagation. Numerical models which are set up using lidar-scanned geometries offer deep insights into failure mechanisms, enabling optimization of 3D printed samples. These models facilitate efficient, small-scale experiments to study anisotropic behavior, surface defects, and applications in larger structures, supporting improved design processes in 3D printed concrete.

2 GOVERNING EQUATIONS

Creating LDPM internal structure starts by inserting particles that represent the coarser aggregate pieces in the concrete specimen. These particles are randomly generated based on a given particle size distribution function (such as the Fuller curve) that suits the concrete’s mix design. A particle generation algorithm ensures there are no overlaps between the newly created particle and previously added particles and the surface nodes of the specimen (Fig. 1a).

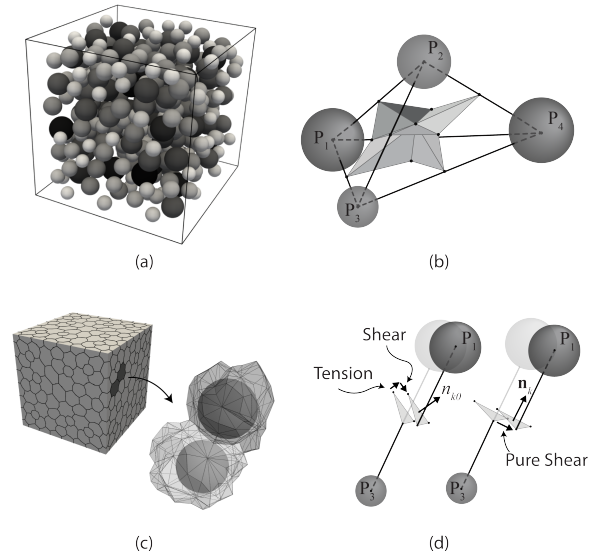


Figure 1: (a) LDPM particles in a cubic geometry following placement procedure; (b) set of four LDPM particles and associated facets; (c) set of two LDPM polyhedral cells composed of a single particle and their surrounding facets; (d) set of two facets interacting in tension-shear and pure shear.

Subsequently, Delaunay tetrahedralization is carried out using particle center position to create a mesh of tetrahedra (Fig. 1b). The tetrahedral mesh defines the lattice system and provides the connections between particles. The next stage involves identifying potential failure and damage locations at the selected length scale. A tessellation process is performed to determine the surfaces through which interaction forces are exchanged between adjacent particles (Fig. 1c). The tessellation of a tetrahedron is obtained by a set of triangles in which each triangle is formed by a point on a tetrahedron edge, a point on a tetrahedron face, and a point inside the tetrahedron (Fig. 1b). At the end of this procedure, a set of polyhedral cells, each including one aggregate piece, is obtained (Fig. 1b). For full description of LDPM geometry, see Ref. [6, 7].

The interaction between particles is simulated through lattice struts. The mechanical interaction on the lattice strut facet is characterized by both normal and shear tractions. These tractions are calculated using strain measures (Equation 1) that computed at the centroid of each facet k through a displacement jump, $[[\mathbf{u}]]_k$

such as,

$$\mathbf{e}_k = \frac{1}{l_k} \mathbf{P}_k \cdot \llbracket \mathbf{u} \rrbracket_k \quad (1)$$

where $\llbracket \mathbf{u} \rrbracket_k = \mathbf{u}_J + \boldsymbol{\theta}_J \times \mathbf{c}_k^J - \mathbf{u}_I - \boldsymbol{\theta}_I \times \mathbf{c}_k^I$, l_k is the tetrahedron edge length connecting particles I and J . Here \mathbf{u} and $\boldsymbol{\theta}$ denote translational and rotational degrees of freedom. $\mathbf{P}_k = [\mathbf{n}_k \ \mathbf{m}_k \ \mathbf{l}_k]^T$, and \mathbf{n}_k , \mathbf{m}_k and \mathbf{l}_k define the appropriate orthonormal vectors of the local reference system (Fig.1d). The normal vector \mathbf{n}_k is aligned with the straight connection of nodes I and J , the tangential vectors can be chosen arbitrarily. The vector \mathbf{c}_k^I points from the node I to the centroid of the k th facet.

Equilibrium is enforced using the linear and angular momentum balance equations of each polyhedral cell as in Equations (2)

$$\sum_{k \in \mathcal{F}_I} A_k \mathbf{P}_k^T \cdot \mathbf{t}_k + V_I \mathbf{b}_I = \mathbf{M}_u^I \cdot \ddot{\mathbf{u}}_I + \mathbf{M}_\theta^I \cdot \ddot{\boldsymbol{\theta}}_I \quad (2a)$$

$$\sum_{k \in \mathcal{F}_I} A_k \mathbf{c}_k^I \times (\mathbf{P}_k^T \cdot \mathbf{t}_k) + V_I \mathbf{r}_I \times \mathbf{b}_I = \mathbf{I}_u^I \cdot \ddot{\mathbf{u}}_I + \mathbf{I}_\theta^I \cdot \ddot{\boldsymbol{\theta}}_I \quad (2b)$$

where \mathcal{F}_I contains all facets of a polyhedral cell I , $A_k = A_{0k} \mathbf{n}_k \cdot \mathbf{n}_{k0}$ is the projected area of a facet orthogonal to the corresponding tetrahedron edge, \mathbf{n}_{k0} is the true normal to the facet plane, V_I is the cell volume, \mathbf{r}_I is the vector from the particle center to the cell centroid, \mathbf{b}_I is the external body force, \mathbf{t}_k is the traction vector in local reference system, and \mathbf{M}_u^I , \mathbf{M}_θ^I , \mathbf{I}_u^I , and \mathbf{I}_θ^I are inertia tensors of the cell, respectively.

The LDPM governing equations are then completed by a set of vectorial constitutive equations relating tractions and strains: $\mathbf{t} = \mathbf{T}(\mathbf{e})$. In the elastic regime one has $\mathbf{t} = \mathbf{E} \cdot \mathbf{e}$ where $\mathbf{E} = E_0 \mathbf{diag}(1 \ \alpha \ \alpha)$ where E_0 and α are model parameters known as effective normal modulus and shear-normal coupling parameter.

2.1 Fracturing behavior

Fracturing behavior occurs when the normal strains are positive ($e_N > 0$). Traction compo-

nents are obtained [11];

$$t_N = \frac{t}{e} e_N; \quad t_M = \alpha \frac{t}{e} e_M; \quad t_L = \alpha \frac{t}{e} e_L \quad (3)$$

The effective stress $t = [t_N^2 + (t_M^2 + t_L^2)\alpha]^{1/2}$ is assumed to be incrementally elastic, $\dot{t} = E_0 \dot{e}$, and it should satisfy the inequality $0 \leq t \leq \sigma_{bt}(\epsilon, \omega)$, where $\sigma_{bt}(e, \omega)$ is a strain-dependent boundary and it can be expressed as:

$$\sigma_{bt}(e, \omega) = \sigma_0(\omega) \exp\left[-H_0(\omega) \frac{\langle \epsilon_{max} - \epsilon_0(\omega) \rangle}{\sigma_0(\omega)}\right] \quad (4)$$

where the brackets $\langle x \rangle = \max(x, 0)$. This boundary σ_{bt} undergoes exponential evolution in relation to the maximum effective strain attained $e_{max} = (e_{N,max}^2 + \alpha e_{T,max}^2)^{0.5}$. The coupling variable, ω , denotes the degree of interaction between shear and normal loading which can be expressed as:

$$\tan \omega = \frac{e_N}{\sqrt{\alpha} e_T} = \frac{t_N \sqrt{\alpha}}{t_T} \quad (5)$$

The function $\sigma_0(\omega)$ is the strength limit for the effective stress and is defined as

$$\sigma_0(\omega) = \sigma_t \frac{-\sin(\omega) + \sqrt{\sin(\omega)^2 + 4\alpha \cos(\omega)^2 / r_{st}^2}}{2\alpha \cos(\omega)^2 / r_{st}^2} \quad (6)$$

where r_{st} is the ratio between the shear strength and the tensile strength, $r_{st} = \sigma_s / \sigma_t$, H_0 is the softening modulus, which is assumed to follow a power function of the internal variable ω and expressed as,

$$H_0(\omega) = H_s / \alpha + (H_t - H_s / \alpha) (2\omega / \pi)^{n_t} \quad (7)$$

where $H_t = 2E_0 / (l_t / l - 1)$ and $l_t = 2E_0 G_t / \sigma_t^2$. G_t is the fracture energy, and l is the length of the tetrahedron edge corresponding to the current facet. $H_s = r_s E_0$. In most cases, $r_s = 0$.

2.2 Compressive behavior

For compressive behavior ($e_N < 0$), the normal stress satisfies the inequality $-\sigma_{bc}(e_D, e_V) \leq t_N \leq 0$ [11]. The normal stress t_N is assumed to be incrementally elastic within

the boundary, $\dot{t}_N = E_{Nc}\dot{\epsilon}_N$. E_{Nc} is the loading-unloading stiffness that increases during unloading. The boundary limit of compressive behavior, $\sigma_{bc}(e_D, e_V)$, is assumed to be a function of the volumetric strain e_V and the deviatoric strain e_D . The compressive boundary can be expressed as

$$\sigma_{bc} = \left\{ \begin{array}{ll} \sigma_{c0} & -e_{DV} \leq 0 \\ \sigma_{c0} + \langle -e_{DV} - \epsilon_{c0} \rangle H_c & 0 \leq -e_{DV} \leq \epsilon_{c1} \\ \sigma_{c1} \exp[(-e_{DV} - \epsilon_{c1})H_c/\sigma_{c1}] & \text{otherwise} \end{array} \right\}$$

where $e_{DV} = e_V + \beta e_D$ (β is a material parameter) and $\epsilon_{c0} = \sigma_{c0}/E_0$ is the compaction strain at the beginning of the pore collapse, $\epsilon_{c1} = \kappa_{c0}\epsilon_{c0}$ is the compaction strain at which rehardening begins, κ_{c0} is the material parameter governing the rehardening and $\sigma_{c1}(r_{DV}) = \sigma_{c0} + (\epsilon_{c1} - \epsilon_{c0})H_c(r_{DV})$.

$H_c(r_{DV})$ is the initial hardening modulus and can be formulated as

$$H_c(r_{DV}) = \frac{H_{c0} - H_{c1}}{1 + \kappa_{c2} < r_{DV} - \kappa_{c1} >} + H_{c1} \quad (8)$$

where H_{c1} is calibrated with experimental data and the strain ratio r_{DV} is calculated as

$$r_{DV} = \begin{cases} -\frac{|\epsilon_D|}{\epsilon_V - \epsilon_{V0}}, & \epsilon_V \leq 0 \\ \frac{|\epsilon_D|}{\epsilon_{V0}}, & \epsilon_V > 0 \end{cases}$$

with $\epsilon_{V0} = 0.1\epsilon_{c0}$.

2.2.1 Frictional behavior

In the compression case, the shear strength increases due to frictional effect. The frictional phenomena simulated by classical incremental plasticity, such as: $\dot{\sigma}_M = E_T(\dot{\epsilon}_M - \dot{\epsilon}_M^p)$, $\dot{\sigma}_L = E_T(\dot{\epsilon}_L - \dot{\epsilon}_L^p)$. The plastic strain increments are assumed to obey the normality rule $\dot{\epsilon}_M = \dot{\lambda}\partial\phi/\partial\sigma_M$, $\dot{\epsilon}_L = \dot{\lambda}\partial\phi/\partial\sigma_L$. The plastic potential can be expressed as $\phi = \sqrt{\sigma_M^2 + \sigma_L^2} - \sigma_{bs}(\sigma_N)$, where the shear strength σ_{bs} is calculated as [11]

$$\sigma_{bs} = \sigma_s + (\mu_0 - \mu_\infty)\sigma_{N0} - \mu_\infty\sigma_N - (\mu_0 - \mu_\infty)\sigma_{N0} \exp(\sigma_N/\sigma_{N0}) \quad (9)$$

where σ_s is the cohesion (shear strength), μ_0 and μ_∞ are the initial and final friction coefficients, and σ_{N0} is the normal stress at which the friction coefficient transitions from μ_0 to μ_∞ .

3 NUMERICAL SIMULATIONS

A computational framework for 3D-printed concrete is developed and calibrated. This framework incorporates mechanical characterization data from experiments and geometric data from lidar scans of printed concrete to predict meso-scale concrete failure. This computational approach aims to reduce laboratory testing requirements, potentially leading to significant reductions in time, cost, and embodied carbon.

3.1 Model Parameters and Calibration

Calibration of the model requires two sets of parameters, the first being associated with properties of the concrete meso-structure. These include the cement content, c , water-cement ratio, $w/c = 0.16$, air volume fraction, ($v_{\text{air}} = 0$), and Fuller coefficient, $n_F = 0.5$, as well as maximum size of aggregate, $d_{\text{max}} = 2\text{mm}$, and minimum particle size used in simulation, $d_{\text{min}} = 1\text{mm}$. This first set of parameters can be obtained directly from the concrete mix design.

The second set of parameters are relevant to the facet constitutive law at the meso-scale level and can be calibrated from load-displacement response of experiments such as compression and fracture tests. In this study, three simulations including uniaxial compression, notched three-point bending and tensile splitting tests are chosen to identify material parameters, and numerically obtained results are directly compared with experimental data from cast specimens.

Obtained results are given as seen in Fig. 2. Numerical results showed good alignment for compressive and fracture test, while tensile splitting test obviously requires further calibration. Parameters calibrated from these test are given in Table 3.1.

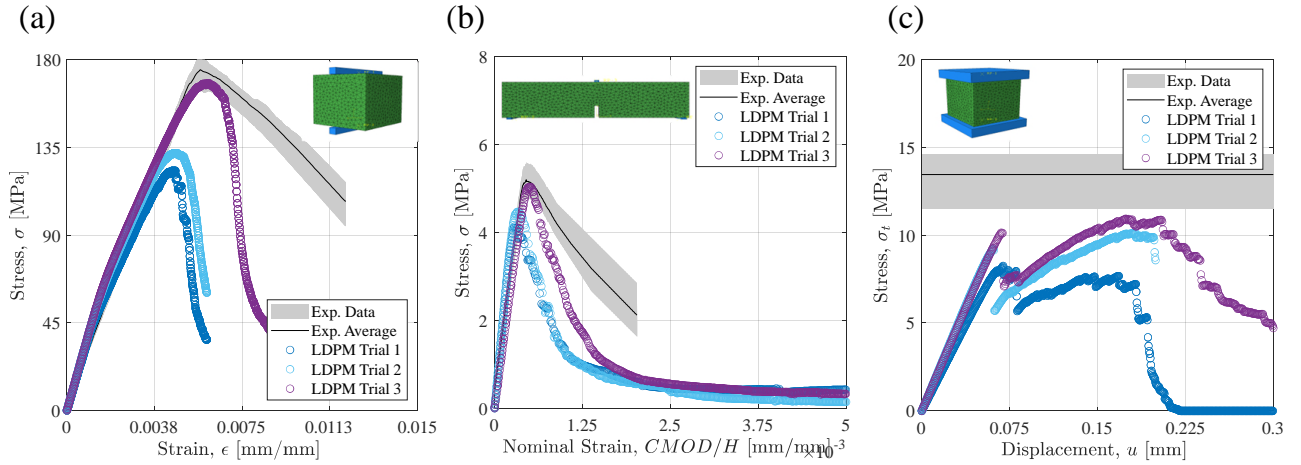


Figure 2: LDPM Parameter Calibration: (a) uniaxial unconfined compression, (b) notched three-point bending, (c) tensile splitting

Table 1: LDPM Parameters

Parameter	-
E_0 [MPa]	75,000
α [-]	0.25
σ_t [MPa]	15
l_t [mm]	10.6
Shear Strength Ratio [-]	6.5
Softening Exponent [-]	0.28
Initial Friction [-]	0.0335

- The marching cubes algorithm [14] generates uniform meshes, ensuring smooth particle placement and reducing vertex clustering.

3.2 Meshing for LiDAR-Scanned Geometries

To account for geometric effects, LiDAR scanning was employed to capture the actual shapes of printed specimens with high precision (accuracy of 0.08 mm). Pre-processing of raw data involved the following steps:

- Point cloud data is merged into a single layer and improving resolution (0.2–0.4 mm) and prepares for triangulation.
- Unwanted artifacts are removed, and the mesh is made watertight using the screened Poisson surface reconstruction algorithm [12].
- Resolution is reduced using quadratic edge collapse decimation [13].

After improving and smoothing 3D scanned geometry, mesoscale internal structure of specimen is created using preprocessor called NU-FreeCAD. Through various Python scripts, the particle placement, meshing, and tessellation procedures outlined in Ref. [6] have been performed. LDPM polyhedral cell structures, tetrahedral mesh, and corresponding facet data are provided as output files that can be read and interpreted by the solver. The NU-FreeCAD Preprocessor is distributed freely¹ under the BSD 3-Clause License. Figure 3 illustrates the mesh generation process and the influences of geometric features.

¹github.com/Concrete-Chrono-Development/chrono-preprocessor

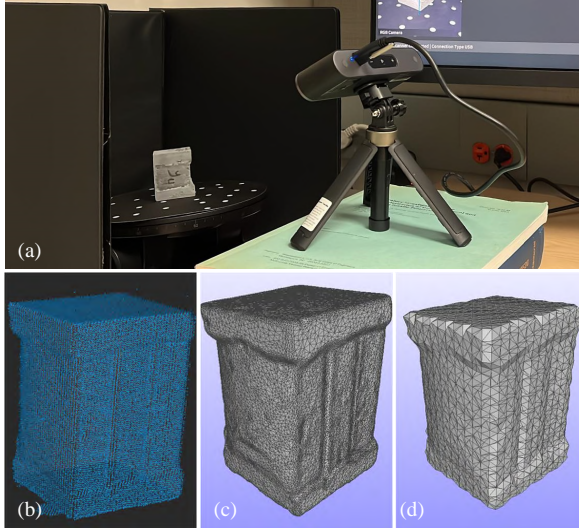


Figure 3: Mesh pre-processing steps: (a) lidar scanning, (b) extracting point cloud, (c) mesh simplification, and (d) mesh regularization.

3.3 Numerical Model Creation

Creating a computational model that accurately represents laboratory experiments for 3D-printed concrete involves addressing several challenges and taking essential steps. One critical step is ensuring smooth and parallel surfaces, especially where the LDPM flat sections of the mesh interact with rigid bodies. This is typically achieved through mesh simplification to minimize noise and scatter from lidar data, see Fig. 4. Another important consideration is determining appropriate interactions, such as evaluating contact properties between loading platens and LDPM mesh. This may involve options like general contact or surface-to-surface contact modeling. Additionally, notches in three-point bending specimens must be added during post-processing of the mesh. This step is necessary because lidar scanners often fail to capture the full notch depth, leading to inaccuracies. Finally, tensile splitting tests present unique challenges, as uncapped surfaces with irregular shapes can cause stress concentrations, Fig. 4d. Addressing this may require modifying the mesh or modeling materials that conform to the concrete's shape. These steps are crucial to creating a reliable computational model for 3D-printed concrete experiments.

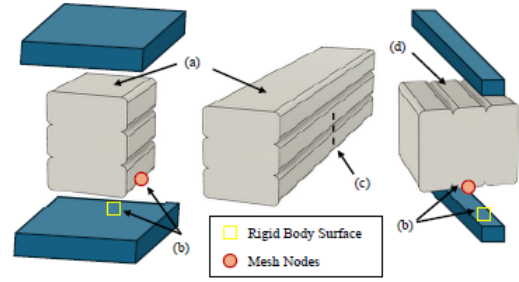


Figure 4: Elements of model setup for simulations: (a) smooth loading surfaces, (b) interaction properties, (c) implementation of notch in mesh, and (d) irregular loading surfaces.

4 RESULTS

A uniaxial compressive test simulation is performed on a 3D-printed sample. The sample, consisting of three layers, has an average length ranging from 29 to 32 mm. It is positioned between caps with dimensions of 40 mm in length, 35 mm in width, and 10 mm in thickness. The total height, measured from the top of the upper cap to the bottom of the lower cap, is 50 mm. During the experiment, a displacement rate of 0.003 mm/s is applied. Obtained result for numerical analysis is given in Fig. 5.

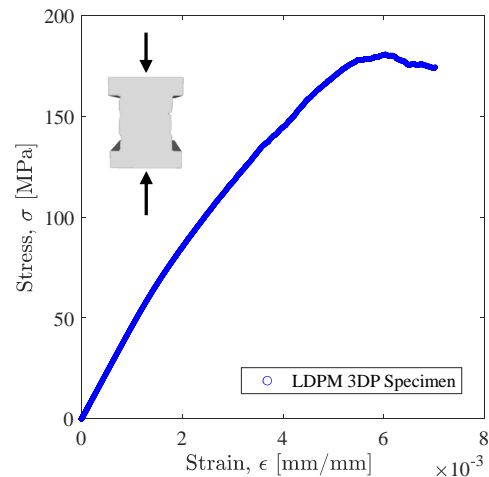


Figure 5: Stress-strain diagram for uniaxial compressive test simulation

5 CONCLUSIONS

This study demonstrates the potential of LDPM simulations combined with lidar-scanned geometries to capture the mechanical

behavior of 3D printed UHPC. By integrating experimental data and numerical modeling, the framework provides valuable insights into the role of anisotropy and surface geometry on the behavior of the 3D printed samples. This study develops a modeling framework which will facilitate prediction of performance of 3D printed samples and provide insight into design decisions for structural applications of 3D printed concrete. Future work includes extending the model to fiber-reinforced specimens and scaling up to structural applications.

REFERENCES

- [1] A. Baktheer and M. Classen, “A review of recent trends and challenges in numerical modeling of the anisotropic behavior of hardened 3D printed concrete”, *Additive Manufacturing*, p. 104309, 2024.
- [2] T. Mader, M. Schreter-Fleischhacker, O. Shkundalova, M. Neuner, and G. Hofstetter, “Constitutive modeling of orthotropic nonlinear mechanical behavior of hardened 3D printed concrete”, *Acta Mechanica*, vol. 234, no. 11, pp. 5893–5918, 2023.
- [3] J. Xiao, H. Liu, and T. Ding, “Finite element analysis on the anisotropic behavior of 3D printed concrete under compression and flexure”, *Additive Manufacturing*, vol. 39, p. 101712, 2021.
- [4] P. Valle-Pello, F. P. Alvarez-Rabanal, M. Alonso-Martinez, and J. del Coz Diaz, “Numerical study of the interfaces of 3d-printed concrete using discrete element method”, *Materialwissenschaft Und Werkstofftechnik*, vol. 50, no. 5, pp. 629–634, 2019.
- [5] Y. Chen, K. Jansen, H. Zhang, C. R. Rodriguez, Y. Gan, O. C. opuro ̇glu, and E. Schlangen, “Effect of printing parameters on interlayer bond strength of 3d printed limestone-calcined clay-based cementitious materials: An experimental and numerical study”, *Construction and Building Materials*, vol. 262, p. 120094, 2020.
- [6] G. Cusatis, D. Pelessone, and A. Mencarelli, “Lattice discrete particle model (LDPM) for failure behavior of concrete. I: Theory”, *Cement and Concrete Composites*, vol. 33, no. 9, pp. 881–890, 2011.
- [7] G. Cusatis, A. Mencarelli, D. Pelessone, and J. Baylot, “Lattice discrete particle model (LDPM) for failure behavior of concrete. II: Calibration and validation”, *Cement and Concrete Composites*, vol. 33, no. 9, pp. 891–905, 2011.
- [8] M. Alnaggar, G. Cusatis, and G. Di Luzio, “Lattice discrete particle modeling (LDPM) of alkali silica reaction (ASR) deterioration of concrete structures,” *Cement and Concrete Composites*, vol. 41, pp. 45–59, 2013.
- [9] E. Lale, R. Rezakhani, M. Alnaggar, G. Cusatis, ”Homogenization coarse graining (HCG) of the lattice discrete particle model (LDPM) for the analysis of reinforced concrete structures”, *Engineering Fracture Mechanics*, 197, 259-277, 2018.
- [10] J. Smith, G. Cusatis, D. Pelessone, E. Landis, J. O’Daniel, and J. Baylot, “Discrete modeling of ultra-high-performance concrete with application to projectile penetration,” *International Journal of Impact Engineering*, vol. 65, pp. 13–32, 2014.
- [11] E. Lale, K. Yu, M. Troemner, J. Elias, M. Stredulova, T. Xue, I. Koutromanos, B. Ayhan, G. Pijaudier-Cabot, J. Khoury, D. Toussaint, A. Tasora, M. Pathirage, Y. Lyu, M. Alnaggar, G. D. Luzio, L. Yang, L. Shen, and G. Cusatis, “On the Computation of the Lattice Discrete Particle model (LDPM) Response with Various Time Integration Solvers”, *SPREE INTERNAL REPORT No. 4-3/4480*. Department of Civil, Environmental Engineer-

ing, Center for Science, and Protection of Engineered Environments (SPREE), Northwestern University, 2024.

[12] M. Kazhdan and H. Hoppe, "Screened Poisson Surface Reconstruction", *ACM Transactions on Graphics (ToG)*, vol. 32, no. 3, 2013.

[13] M. Garland and P. S. Heckbert, "Sur-

face Simplification Using Quadric Error Metrics", *Proceedings of the 24th Annual Conference on Computer Graphics and Interactive Techniques*, 1997.

[14] C. Maple, "Geometric Design and Space Planning Using the Marching Squares and Marching Cubes Algorithms", *2003 International Conference on Geometric Modeling and Graphics*, IEEE, 2003.